Applied Thermal Engineering 265 (2025) 125536

Contents lists available at ScienceDirect

Applied Thermal Engineering

journal homepage: www.elsevier.com/locate/ate

Research Paper

Shape uncertainty analysis of laminar forced convection in a round microchannel with viscous dissipation

A. Barletta [a,*], M. Celli [a], L.A. Sphaier [b], P.V. Brandão [a], S. Lazzari [c], E. Ghedini [a]

[a] Department of Industrial Engineering, Alma Mater Studiorum Università di Bologna, Viale Risorgimento 2, 40136 Bologna, Italy
[b] Department of Mechanical Engineering, Universidade Federal Fluminense, Rua Passo da Pátria 156, sala 302, bloco D, Niterói, RJ, Brazil
[c] Department of Architecture and Design, Università degli Studi di Genova, Stradone di S.Agostino 37, 16128 Genova, Italy

ARTICLE INFO

Keywords:
Laminar flow
Forced convection
Microchannel
Viscous dissipation
Sensitivity analysis
Friction factor
Nusselt number

ABSTRACT

This paper is aimed at analysing the effects of roughness caused by random geometric uncertainties in microchannels and how these can influence heat transfer and pressure drop in fluid flow within such geometries. The shape of a microchannel is typically affected by significant uncertainty due to the small size of the cross-section, which is comparable to the typical wall-roughness length scale. While this uncertainty exists at any scale, it becomes amplified and critically important when the hydraulic diameter is smaller than a few tens of micrometer. The analysis is performed numerically, considering a nominally circular channel with random variations in its cross-section within a prefixed maximum extent, effectively representing roughness at the micro-scale. The adopted mathematical model considers fully developed heat and fluid flow by taking into account the effect of viscous dissipation and an irregular cross-section is generated by random geometric variations. The effects of an increasing wall roughness generally lead to an increase in the Fanning friction factor and a decrease in the wall heat transfer rate, as expressed by the Nusselt number.

1. Introduction

Forced convection flows in microchannels are of great interest for the applications in the field of thermal management [1]. For instance, an important application is the regenerative cooling of combustion chamber liners, where large heat flux removal at diverse operation temperatures may occur. Furthermore, studies of microfluidics and microscale heat transfer have a big impact on the cryogenic cooling employed for the supercomputing chips. Cooling of concentrator photovoltaics via microchannel fluid flows turned out to be an innovative application, as pointed out by Gilmore et al. [2].

Miniaturization of the heat exchangers for several energy and heat transfer applications often entails the use of microchannels. A significant uncertainty can affect the shape of a microchannel cross-section due to the small hydraulic diameter [3,4]. When the hydraulic diameter becomes smaller than some tens of micrometer, the shape uncertainty induced by the wall roughness, and present at any scale, becomes significantly important. The focus of this paper is on the numerical analysis of the sensitivity to shape random modifications, within a prefixed maximum extent, of the main flow and heat transfer characteristics of fully-developed forced convection with viscous dissipation. The study includes the evaluation of the Fanning friction factor and of the Nusselt number for the T, H1 and H2 thermal boundary conditions.

While there is a wide literature regarding the effect of viscous dissipation on the forced convection analysis of microchannels [5–10], there is little information regarding the effects of random departures from the average shape of the cross-section . Such departures are expected to be important due to the roughness of the solid wall, which depends on the manufacturing techniques and on the surface treatment of the materials [11]. Their effects lead to uncertainties in the significant parameters characteristic of the forced convection flow and heat transfer. The originality of this study is the numerical character of the analysis carried out by a finite-element solver on a domain where the boundary is randomly modified with respect to the circular shape.

We point out that considering a random geometry as a model of wall roughness appears to be an interesting approach. Many authors model the wall roughness via regular geometric patterns, as in the study by Wang and Wang [12] where the wall roughness is represented through periodic wall functions. A similar approach can also be found in Turgay and Yazicioglu [13] and in Croce et al. [14] where regular distributions of conical peaks have been envisaged. Random generation of peaks and valleys of rectangular shape was carried out in the computational study by Croce and D'Agaro [15]. Our study departs from such investigations by a different approach to the wall-roughness model where a random polygonal path is employed to generate the

* Corresponding author.
E-mail address: antonio.barletta@unibo.it (A. Barletta).

https://doi.org/10.1016/j.applthermaleng.2025.125536
Received 19 October 2024; Received in revised form 16 December 2024; Accepted 10 January 2025
Available online 17 January 2025

Nomenclature

a	Constant temperature gradient
Br	Brinkman number
c	Specific heat
f	Fanning friction factor
k	Thermal conductivity
$\mathbf{n}$	Unit normal vector
Nu	Nusselt number
p	Pressure
$\mathcal{P}$	Cross-sectional perimeter
q_w	Average wall heat flux
$\dot{Q}$	Thermal power supplied at the wall
r	Radial coordinate
r_h	Hydraulic radius of the microchannel
r_0	Duct radius
Re	Reynolds number
$\mathcal{S}$	Cross-sectional area
T	Temperature
T_b	Bulk temperature
T_w	Average wall temperature
u	Velocity
u_0	Reference velocity
u_m	Mean flow velocity
x, y, z	Cartesian coordinates
Greek symbols	
α	Thermal diffusivity
γ	Maximum relative uncertainty of the boundary radius
Φ	Dissipation function
μ	Dynamic viscosity
ν	Kinematic viscosity
σ	Poiseuille number, $f\,Re$
Subscripts, superscripts	
$\bar{}$	Dimensionless quantity
T, H1, H2	Thermal boundary conditions

microchannel cross-section. Such a procedure is intended to improve the adherence of the model to the actual shape in a real microchannel. We finally note that experimental data assessing the role of wall roughness were reported by Celata et al. [16] relative to the transition from laminar to turbulent regimes.

2. Governing equations

Let us consider a straight round microchannel and allow for an uncertainty in the actual shape of the cross-section, due to the practical manufacturing characteristics whatever is the adopted fabrication technique.

Shape uncertainty issues may be due to the size of the typical surface roughness relative to the small hydraulic diameter of the microchannel. Thus, though the average shape of the microchannel is circular with radius r_0, we will denote the perimeter of the duct cross-section with $\mathcal{P}$ and encircled area with $\mathcal{S}$. More precisely, $\mathcal{P}$ is a closed polygon which matches a circle within a tolerance γ, for $0 < \gamma < 1$, meaning that each point on $\mathcal{P}$ has a distance r from the centre of the cross-section such that $(1-\gamma)\,r_0 < r < (1+\gamma)\,r_0$. Here, γ is a measure of the relative roughness with respect to the radius r_0. We note that the symbols $\mathcal{P}$ and $\mathcal{S}$ will be tacitly employed to denote both the geometric objects and their measures (perimeter and area).

Let (x, y) be the Cartesian coordinates on the cross-sectional plane and z be the streamwise coordinate. The flow is assumed to be laminar, stationary, incompressible and fully-developed, both hydrodynamically and thermally, so that the only nonzero component of the velocity field is that in the z direction, which is denoted by u. Due to the local mass balance equation, *i.e.* the zero-divergence condition on the velocity, u is independent of z, and hence $u = u(x, y)$. Furthermore, the local difference between the pressure and the hydrostatic pressure depends only on z and is denoted by $p(z)$. Under such conditions, the local momentum balance equation is expressed as

$$\nabla^2 u = \frac{1}{\mu}\,\frac{\mathrm{d}p}{\mathrm{d}z}, \tag{1}$$

where $\mathrm{d}p/\mathrm{d}z$ is a constant and μ indicates the dynamic viscosity. Thus, (1) is a two-dimensional partial differential equation defined in the (x, y) plane. Such an equation is subject to the no-slip boundary condition

$$u = 0, \quad (x, y) \in \mathcal{P}. \tag{2}$$

The thermal boundary conditions envisaged in this study are either T, H1 or H2 according to the classification defined by Shah and London [17]. We recall that condition T means a peripherally (along $\mathcal{P}$) and longitudinally (along z) uniform wall temperature, H1 means a peripherally uniform wall temperature and a longitudinally uniform wall heat flux, while H2 means a peripherally and longitudinally uniform wall heat flux (see Fig. 1). It is also well-known that, for symmetry reasons, conditions H1 and H2 coincide when $\mathcal{P}$ is exactly a circle [17]. Furthermore, the boundary conditions T, H1 and H2 imply that the derivative $\partial T/\partial z$ is a constant [17,18], hereafter denoted as a. Thus, in the thermally developed regime, the local energy balance equation is given by [17,18],

$$\alpha\,\nabla^2 T - a\,u + \frac{\nu}{c}\,\Phi = 0, \quad \Phi = |\boldsymbol{\nabla} u|^2, \tag{3}$$

where α, ν and c are fluid properties, namely, the thermal diffusivity, the kinematic viscosity and the specific heat. Moreover, $\Phi = \Phi(x, y)$ is the viscous dissipation function [18]. The importance of the viscous dissipation effect for the local energy balance in a microchannel has been demonstrated by many authors [5–10].

2.1. Dimensionless formulation

Let us define the dimensionless quantities and operators

$$(\bar{x}, \bar{y}) = \frac{(x, y)}{r_0}, \quad \bar{\boldsymbol{\nabla}} = r_0 \boldsymbol{\nabla}, \quad \bar{\nabla}^2 = r_0^2 \nabla^2, \quad \bar{u} = \frac{u}{u_0}, \quad \bar{T} = k\,\frac{T - T_w}{q_w\, r_0}, \tag{4}$$

where k is the thermal conductivity of the fluid and

$$u_0 = -\frac{2 r_0^2}{\mu}\,\frac{\mathrm{d}p}{\mathrm{d}z}, \quad T_w = \frac{1}{\mathcal{P}}\int_{\mathcal{P}} T\,\mathrm{d}\mathcal{P}, \quad q_w = \frac{k}{\mathcal{P}}\int_{\mathcal{P}} \mathbf{n}\cdot\boldsymbol{\nabla} T\,\mathrm{d}\mathcal{P}. \tag{5}$$

Here, T_w and q_w are the peripherally averaged wall temperature and incoming wall heat flux, respectively, while $\mathbf{n}$ is the outward unit normal with respect to the boundary and u_0 is a constant reference velocity such that

$$\frac{u_0}{u_m} = f\,Re = \sigma, \quad u_m = \frac{1}{\mathcal{S}}\int_{\mathcal{S}} u\,\mathrm{d}\mathcal{S}, \tag{6}$$

with u_m being the mean flow velocity, f the Fanning friction factor and $Re = 2\,u_m\,r_0/\nu$ the Reynolds number [17]. We note that the mean wall temperature T_w is a constant, *i.e.*, it is independent of z only when the T boundary condition is selected. With either conditions T, H1 or H2, it is easily proved that the mean wall heat flux q_w is a constant and the constant a not only coincides with $\partial T/\partial z$, but also with $\mathrm{d}T_w/\mathrm{d}z$ and $\mathrm{d}T_b/\mathrm{d}z$, where T_b is the bulk temperature,

$$\frac{\partial T}{\partial z} = \frac{\mathrm{d}T_w}{\mathrm{d}z} = \frac{\mathrm{d}T_b}{\mathrm{d}z} = a, \quad T_b = \frac{1}{\mathcal{S}\,u_m}\int_{\mathcal{S}} T u\,\mathrm{d}\mathcal{S}. \tag{7}$$

In fact, the bulk value of a scalar is nothing but its mean value over the cross-section $\mathcal{S}$ weighted by the velocity profile $u(x, y)$.

On account of (5) and (7), the dimensionless temperature $\bar{T}$ defined by (4) has interesting properties such as

$$\int_{\mathcal{P}} \bar{T}\,\mathrm{d}\mathcal{P} = 0, \quad \frac{\mathrm{d}\bar{T}}{\mathrm{d}z} = 0, \quad \frac{1}{\mathcal{S}\,u_m}\int_{\mathcal{S}} \bar{T} u\,\mathrm{d}\mathcal{S} = -\frac{2}{Nu}, \tag{8}$$

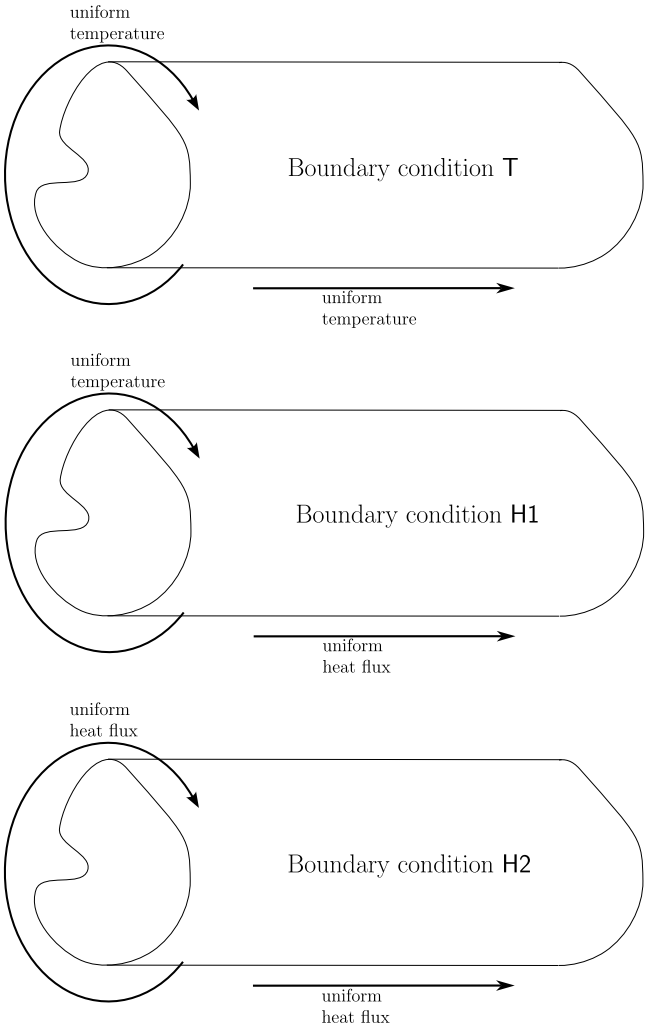

Fig. 1. A schematic description of the T, H1 and H2 thermal boundary conditions for a microchannel with arbitrary cross-sectional shape.

where the Nusselt number Nu is a constant whose definition is given by [17],

$$Nu = \frac{2r_0\, q_w}{k\left(T_w - T_b\right)}. \tag{9}$$

On account of (4), one can rewrite (1) as

$$\bar{\nabla}^2 \bar{u} + \frac{1}{2} = 0, \tag{10}$$

to be solved by employing the boundary condition

$$\bar{u} = 0, \quad (\bar{x}, \bar{y}) \in \bar{\mathcal{P}}. \tag{11}$$

The symbols $\bar{\mathcal{P}}$ and $\bar{\mathcal{S}}$ denote the dimensionless geometric objects obtained from $\mathcal{P}$ and $\mathcal{S}$ with the coordinates scaled by the reference length r_0. After solving (10) and (11), one can evaluate the Poiseuille number $\sigma = f\, Re$ by employing (5) and (6) through the formula

$$\sigma = f\, Re = \frac{\bar{\mathcal{S}}}{\displaystyle\int_{\bar{\mathcal{S}}} \bar{u}\, \mathrm{d}\bar{\mathcal{S}}}. \tag{12}$$

On account of (4), the local energy balance Eq. (3) can be rewritten as

$$\bar{\nabla}^2 \bar{T} - \sigma\, \bar{a}\, \bar{u} + 2\, \sigma^2\, Br\, |\bar{\boldsymbol{\nabla}} \bar{u}|^2 = 0, \tag{13}$$

where Br is the Brinkman number and $\bar{a}$ is a dimensionless parameter,

$$Br = \frac{\mu u_m^2}{2r_0 q_w}, \quad \bar{a} = \frac{k r_0 u_m}{q_w \alpha}\, a. \tag{14}$$

By employing Gauss' theorem together with the definitions given by (4) and (5), an integration of (13) over the dimensionless region $\bar{\mathcal{S}}$ yields an explicit expression of $\bar{a}$, namely

$$\bar{a} = \frac{\bar{\mathcal{P}}}{\bar{\mathcal{S}}} + \frac{2\, \sigma^2\, Br}{\bar{\mathcal{S}}} \int_{\bar{\mathcal{S}}} |\bar{\boldsymbol{\nabla}} \bar{u}|^2\, \mathrm{d}\bar{\mathcal{S}}. \tag{15}$$

The boundary conditions to be satisfied are, alternatively,

$$\bar{T} = 0, \quad (\bar{x}, \bar{y}) \in \bar{\mathcal{P}}, \quad \text{for the boundary condition T}, \tag{16}$$

$$\bar{T} = 0, \quad (\bar{x}, \bar{y}) \in \bar{\mathcal{P}}, \quad \text{for the boundary condition H1}, \tag{17}$$

$$\mathbf{n} \cdot \bar{\boldsymbol{\nabla}} \bar{T} = 1, \quad (\bar{x}, \bar{y}) \in \bar{\mathcal{P}}, \quad \int_{\bar{\mathcal{P}}} \bar{T}\, \mathrm{d}\bar{\mathcal{P}} = 0, \quad \text{for the boundary condition H2}. \tag{18}$$

The steps to be followed for every assignment of the cross-sectional region $\bar{\mathcal{S}}$ are the following:

1. Solve (10) and (11) for the dimensionless velocity profile $\bar{u}(\bar{x}, \bar{y})$;
2. Evaluate σ by using (12);
3. The local energy balance Eq. (13) must be solved for the dimensionless temperature profile $\bar{T}(\bar{x}, \bar{y})$ with a boundary condition given either by (16), (17) or (18).

We stress that the distinction between the boundary conditions T and H1 relies in $\bar{a}$ being zero for the T case and generally nonzero for the H1 case.

Table 1
Accuracy test of the numerical solution for the boundary condition T.

MaxCellMeasure	σ	Nu	Br
0.01	18.1841	6.52915	−0.164093
0.005	18.1253	6.53210	−0.164625
0.001	18.0383	6.53633	−0.165419
0.0005	18.0181	6.53668	−0.165605
0.0001	17.9952	6.53673	−0.165815
0.00005	17.9912	6.53669	−0.165853

2.1.1. Boundary condition T

With the boundary condition T, the Brinkman number is unknown a priori, while $\bar{a}$ must be set equal to 0. Thus, (15) serves to determine the value of Br to be employed in the solution of (13) and (16),

$$Br = -\frac{\bar{\mathcal{P}}}{2\sigma^2 \int_{\bar{S}} |\bar{\nabla}\bar{u}|^2 \, \mathrm{d}\bar{S}}. \tag{19}$$

Eq. (19) shows that the value of Br is always negative. Physically, this means that an outgoing wall heat flux is needed ($q_w < 0$) to counterbalance the internal heating effect of viscous dissipation and, hence, to maintain a uniform wall temperature.

2.1.2. Boundary conditions H1 and H2

In the cases H1 and H2, Br is an input parameter with any arbitrary value and $\bar{a}$ is to be evaluated by employing (15) prior to the solution of (13) with either conditions (17) or (18). It is important to recall that in the special case where the uncertainty in the exact shape of the duct cross-section is zero, namely the case where $\bar{S}$ is the unit disk, the two boundary conditions H1 and H2 coincide [17]. This is a consequence of the special geometrical symmetry of the circle, which is broken in the presence of surface roughness.

2.2. Evaluation of the Nusselt number

After taking the above described steps towards the determination of $\bar{u}$ and $\bar{T}$, one can finally evaluate Nu by using (6)–(8), namely

$$Nu = -\frac{2\bar{S}}{\sigma \int_{\bar{S}} \bar{T}\,\bar{u}\,\mathrm{d}\bar{S}}. \tag{20}$$

2.3. A perfectly smooth round microchannel

Recalling the well-known results relative to an exactly circular cross-section may be useful for the forthcoming discussion of the results. In the absence of any roughness, the dimensionless velocity is given by the Hagen–Poiseuille profile,

$$\bar{u} = \frac{1}{8}\left(1 - \bar{r}^2\right), \tag{21}$$

with $\bar{r} = \sqrt{\bar{x}^2 + \bar{y}^2}$. Moreover,

$$\bar{S} = \pi, \quad \bar{\mathcal{P}} = 2\pi. \tag{22}$$

Thus, (12) and (15) yield

$$\sigma = f\,Re = 16, \quad \bar{a} = 2(1 + 8\,Br). \tag{23}$$

One can now employ (13), (16)–(18) and (20). Then, for the boundary condition T, one has

$$Br = -\frac{1}{8}, \quad \bar{T} = -\frac{1}{4}\left(1 - \bar{r}^4\right), \quad Nu = \frac{48}{5}. \tag{24}$$

For the boundary condition H1 and H2, one has

$$\bar{T} = -\frac{1}{4}\left(1 - \bar{r}^2\right)\left[3 - \bar{r}^2 + 16Br\left(1 - \bar{r}^2\right)\right], \quad Nu = \frac{48}{11 + 48Br}. \tag{25}$$

3. Numerical methodology

The path defining the dimensionless boundary $\bar{\mathcal{P}}$ of the microchannel cross-section $\bar{S}$ is defined by a polygon (see Fig. 2). In fact, polygonal paths connecting 100 points are defined with polar coordinates by randomly generating angles between 0 and 2π and dimensionless radii in the range $1 - \gamma \le \bar{r} \le 1 + \gamma$. Each polygonally bounded microchannel has a dimensionless hydraulic radius given by

$$\bar{r}_h = \frac{2\bar{S}}{\bar{\mathcal{P}}}. \tag{26}$$

Here, $\bar{r}_h \le 1$ with equal sign holding for the smooth circular duct.

The computational domain is the dimensionless region bounded by the polygonal path. Uniform unstructured meshes are generated with triangular elements. The domain and mesh generation is achieved by using the software *Wolfram 14.1* (© Wolfram Research Inc.). Furthermore, the weak formulation of the governing equations and their solution with the finite element method is managed by utilizing the built-in function `NDSolve` of *Wolfram 14.1*. The accuracy of the numerical solution can be tested by inspecting the effect of increasing mesh refinements. Refining the mesh is achieved by assigning the parameter `MaxCellMeasure` within the function `ToElementMesh`.

Fig. 2 illustrates a sample case with $\gamma = 1/10$. An accuracy test can be done with reference to the region displayed in Fig. 2 and for the evaluation of σ, of the Nusselt number and the Brinkmann number corresponding to the T boundary condition. By decreasing the value of `MaxCellMeasure`, one attains accurate results for σ, Nu and Br with at least three significant figures, as shown in Table 1. In order to keep the computational time reasonably small, for each case considered, all the forthcoming results are generated with `MaxCellMeasure` set to 10^{-3}. Table 1 reveals that the computational region deformed with respect to the unit circle yields larger values of σ and $|Br|$, with a smaller value of Nu. Indeed, the effects of a significant wall roughness generally mean a larger wall friction and a larger viscous dissipation, with respect to the case of a smooth tube wall reported in Eqs. (23) and (24). Furthermore, the surface roughness induces a relatively smaller velocity close to the wall resulting in a less efficient heat transfer and, hence, in a smaller Nu.

Contour plots of the dimensionless velocity and temperature fields are reported in Fig. 3, with $\bar{T}(\bar{x}, \bar{y})$ relative to the T boundary condition, and to the H1 and H2 boundary conditions with $Br = 1$. One may note that $\bar{T}(\bar{x}, \bar{y}) \le 0$ in all cases considered in Fig. 3. The reasons are different in the three cases envisaged in this figure. In fact, can deduce from Eqs. (4) and (14), as well as from the considerations given in Section 2.1.1, that for the boundary condition T one has $T(x, y) \ge T_w$ with $Br < 0$ and, hence, $q_w < 0$. On the other hand, for $Br = 1$ and the boundary conditions H1 or H2, one has $T(x, y) \le T_w$ with $q_w > 0$. One may also point out that the contour values of $\bar{u}(\bar{x}, \bar{y})$ displayed in Fig. 3 do not show a strong discrepancy from the maximum value of $\bar{u}$, namely 0.125, predicted by Eq. (21) for the smooth circular duct.

4. Discussion of the results

4.1. Negligible viscous dissipation

A statistical sample of 100 different microchannels is obtained by generating multiple polygonal paths and, hence, multiple computational regions where the values of σ, $\bar{r}_h$ and Nu, for the two cases H1 and H2, are evaluated with reference to the special case $Br \to 0$ by setting $\gamma = 1/100$ and $1/10$. Such values have been reported in Figs. 4 and 5 where, in abscissa, the labels of the 100 different microchannels are given. The analytical values of σ, $\bar{r}_h$, Nu_{H1} and Nu_{H2} for the circular duct are determined according to Eqs. (23)–(26) and they are given for comparison as grey lines, whereas the actual average values are identified as red dashed lines with pink coloured bands showing confidence intervals within 1 standard deviation tolerance.

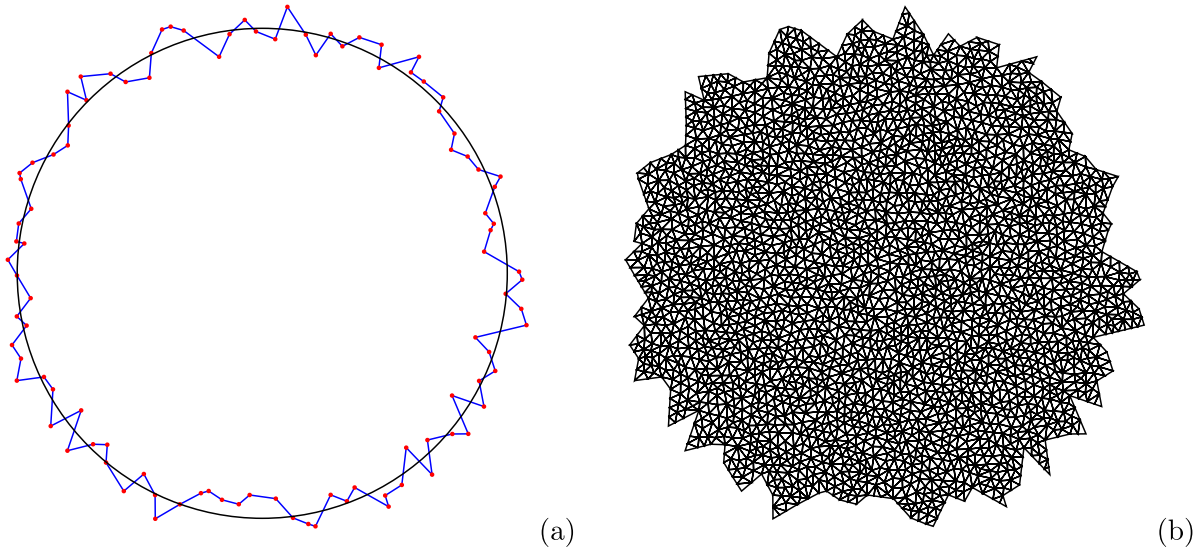

Fig. 2. (a) Sample polygonal approximation of the actual microchannel boundary (blue) as compared to the smooth circular boundary (black); (b) Unstructured mesh with triangular elements for the actual computational domain.

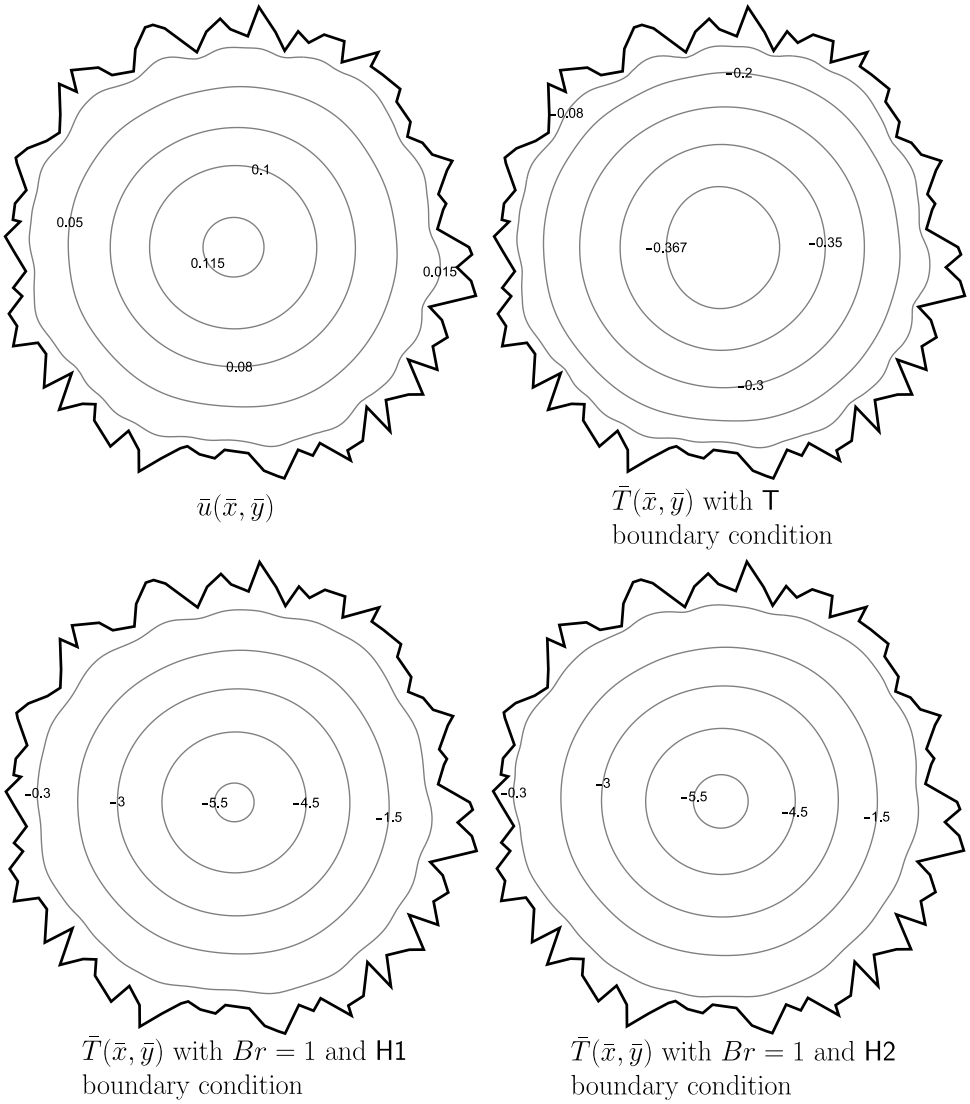

Fig. 3. Contour plots of $\bar{u}(\bar{x},\bar{y})$ and $\bar{T}(\bar{x},\bar{y})$ for the sample case of Fig. 2 with T boundary condition, and with H1 and H2 boundary conditions for $Br = 1$.

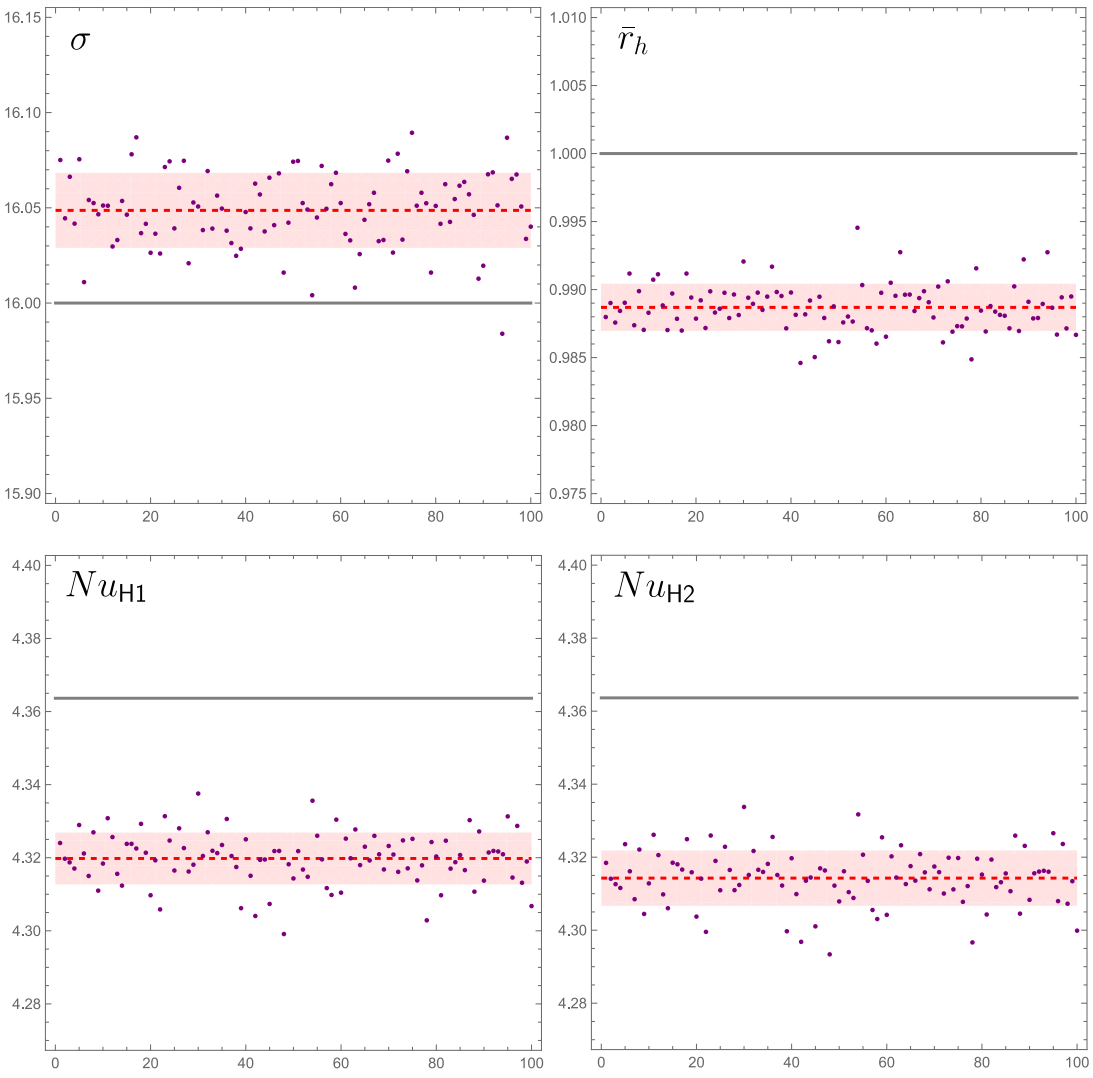

Fig. 4. Case $\gamma = 1/100$: values (purple dots) of σ, $\bar{r}_h$ and, with $Br \to 0$, of Nu_{H1}, Nu_{H2} for 100 different microchannels. The red dashed lines indicate the average values and the pink bands denote the 1 standard deviation range from the average value. The grey lines denote the analytically determined values for the smooth circular microchannel.

In both cases $\gamma = 1/100$ and $\gamma = 1/10$, it turns out that the values obtained analytically for the circular duct are more than one standard deviation away from the average values. Such a result is evident from Figs. 4 and 5. As a consequence, one may infer a systematic effect of the wall roughness, already anticipated when commenting on Table 1. We mention that, if the relative roughness $\gamma = 1/10$ might be considered as unrealistic for macroscale circular ducts, it becomes quite conceivable by downsizing the duct to the microscale. There is a shape sensitivity in the values of σ, $\bar{r}_h$ and Nu which results into a net increase of σ for $\gamma = 1/100$ and, even more, for $\gamma = 1/10$. Strictly speaking, there is just a single case, evident in Fig. 4, where σ is slightly smaller than 16. The increase in σ is due to the augmented hydraulic resistance induced by the wall roughness. A side effect is the lower velocity close to the walls caused by the meandering geometry of the polygonal path enclosing the microchannel cross-section. An illustration of this effect, already mentioned in Section 3, is shown in Fig. 6, where the Hagen–Poiseuille profile (red line) is compared with the averaged dimensionless velocity profile (blue line) over the 100 angular positions employed in the polygonal path shown in Fig. 2. The comparison is made effective by reporting in abscissa the ratio $\bar{r}/\bar{r}_{max}$, where $\bar{r}_{max}$ is equal to 1 for the smooth circular duct while it is equal to the maximum value of $\bar{r}$, namely 1.09883, for the rough microchannel displayed in Fig. 2. Such a velocity depletion effect close to the wall may explain the less efficient wall heat transfer and, hence, the lower Nusselt numbers Nu_{H1} and Nu_{H2} with respect to the smooth circular case, displayed in Figs. 4 and 5. One may mention that the velocity reduction close to the wall competes with the exchange surface increase that tends to enhance the heat transfer rate. As noted by Pelević and van der Meer [19], the reason behind a predicted heat transfer enhancement or reduction remains unclear. In fact, as conjectured by Croce and D'Agaro [20] and by Pelević and van der Meer [19], the heat transfer rate is expected to be unaffected by the surface roughness on the average. However, such a conjecture is not confirmed by the present analysis.

In the case $\gamma = 1/100$ reported in Fig. 4, the mean values of Nu_{H1} and Nu_{H2} lie within the respective confidence intervals (pink bands) meaning that such values can be considered as statistically coincident, exactly as it happens for the smooth circular duct. As γ increases (see Fig. 5), such a conclusion cannot be drawn any more as a net, though minor, difference between Nu_{H1} and Nu_{H2} emerges. Figs. 4 and 5 show that the dimensionless hydraulic radius $\bar{r}_h$ is smaller than unity, as one expects from (26). This result is a consequence of the markedly larger denominator of the fraction $\bar{r}_h$, as compared with the smooth circular path, with a relatively minor change in the numerator, namely the cross-sectional area. Again, such an effect is more important for $\gamma = 1/10$ than for $\gamma = 1/100$.

Fig. 7 systematically shows the monotonic trends for the average values of σ and $\bar{r}_h$ versus γ within their 1 standard deviation ranges. Data displayed in Fig. 7 are not influenced by the heat transfer rate

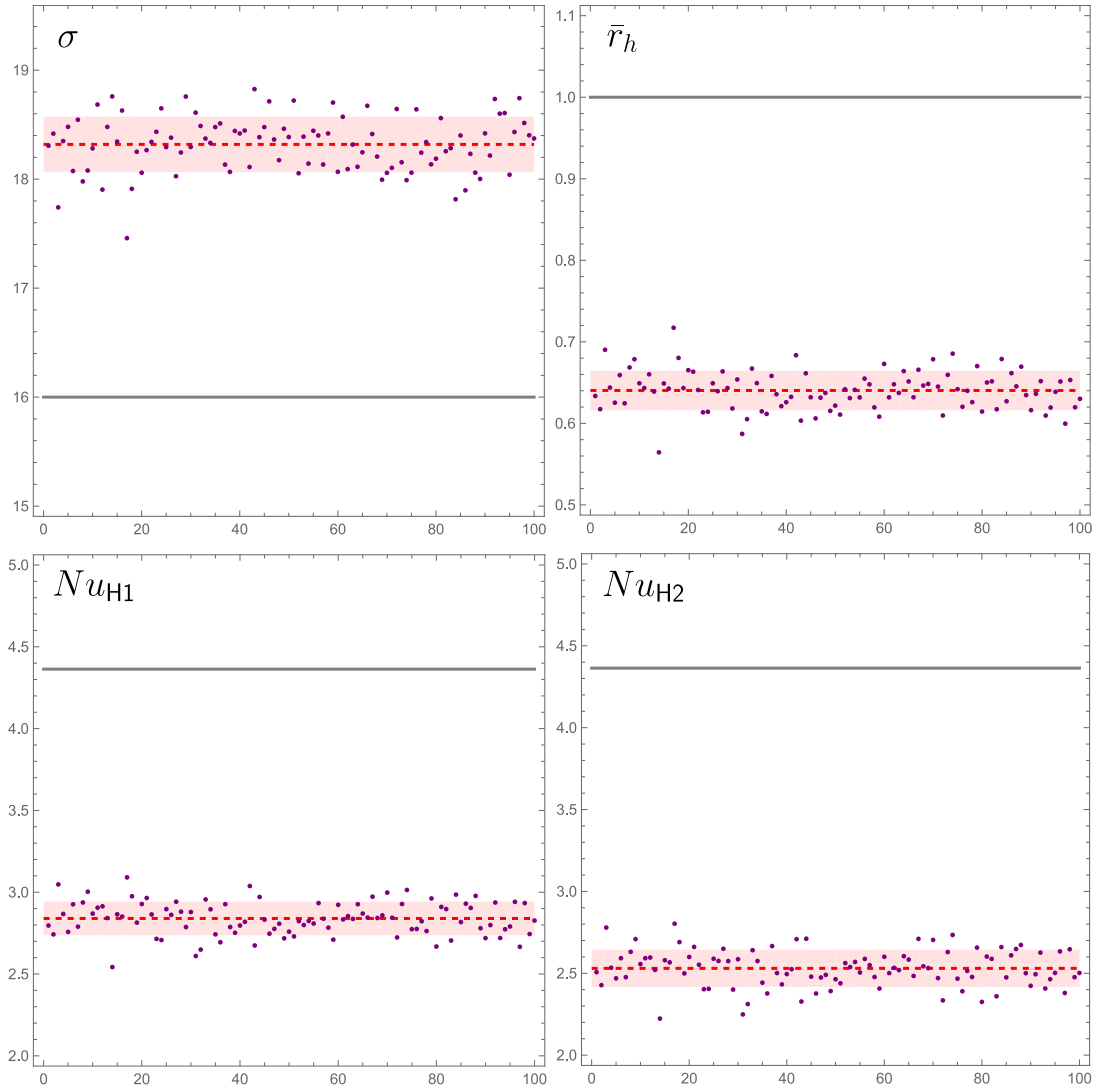

Fig. 5. Case $\gamma = 1/10$: values (purple dots) of σ, $\bar{r}_h$ and, with $Br \to 0$, of Nu_{H1}, Nu_{H2} for 100 different microchannels. The red dashed lines indicate the average values and the pink bands denote the 1 standard deviation range from the average value. The grey lines denote the analytically determined values for the smooth circular microchannel.

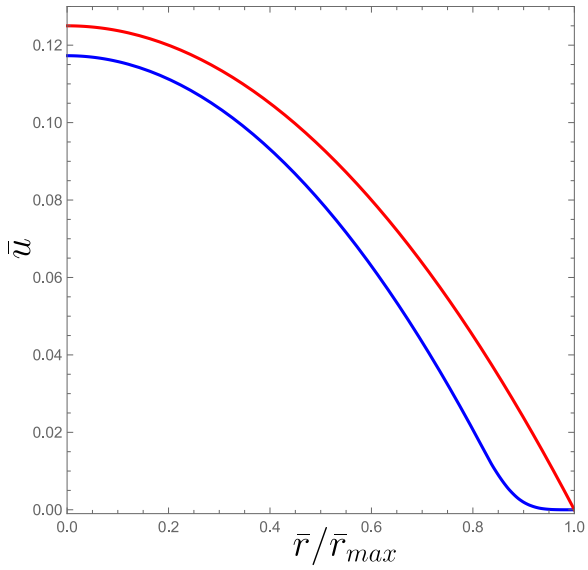

Fig. 6. Average radial velocity profile (in blue) obtained for the computational domain defined in Fig. 2 compared with the Hagen–Poiseuille profile (in red) given by (21).

and the effect of viscous dissipation as we are assuming a regime of forced convection. On the other hand, the heat transfer rate and the role played by viscous dissipation are discussed in the forthcoming Section 4.2. The data for $\gamma = 0$ are those given analytically in Section 2.3. In particular, $\sigma = 16$ and $\bar{r}_h = 1$, with a standard deviation equal to zero. Fig. 7 shows that σ increases and $\bar{r}_h$ decreases over the whole considered range of γ, up to $\gamma = 0.15$. This figure also shows that the standard deviation increases with γ, as it is expected since the shape variability over the statistical sample is more and more pronounced as γ increases.

4.2. The effects of viscous dissipation

On analysing heat transfer, the role played by viscous dissipation becomes important for every type of temperature boundary conditions. However, as already pointed out, the boundary condition T is special as the Brinkman number, in this case, is not an arbitrarily assigned parameter, but its value is uniquely defined through (19). Likewise, for the boundary condition T, also Nu is uniquely determined as a function of the roughness parameter γ.

Fig. 8 shows how the Brinkman number and the Nusselt number are affected by γ, for the boundary condition T. As shown analytically for the round duct in Section 2.3, the value of Br is −0.125 and that of

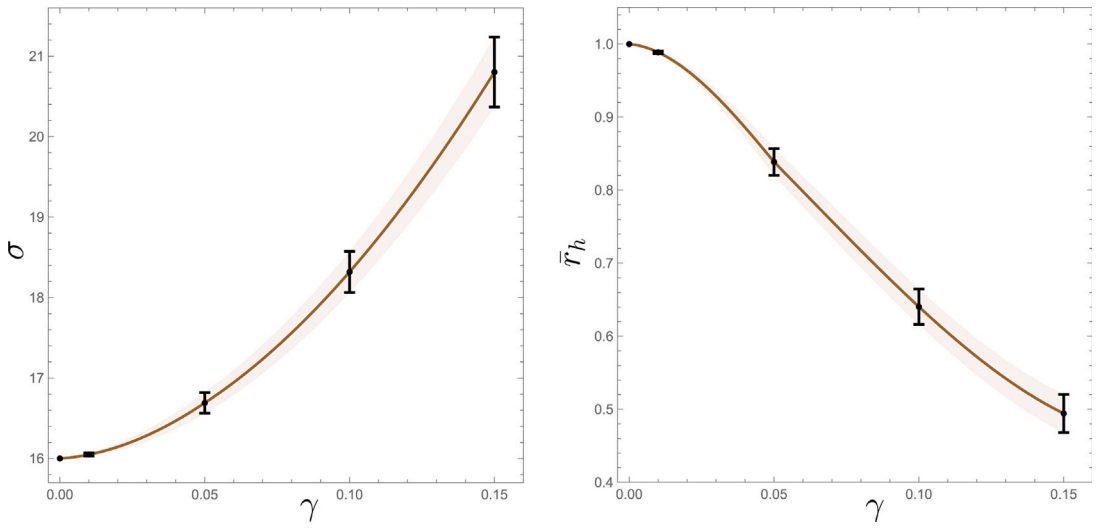

Fig. 7. Values of σ and $\bar{r}_h$ versus γ: average values (black dots) with 1 standard deviation range (black segments).

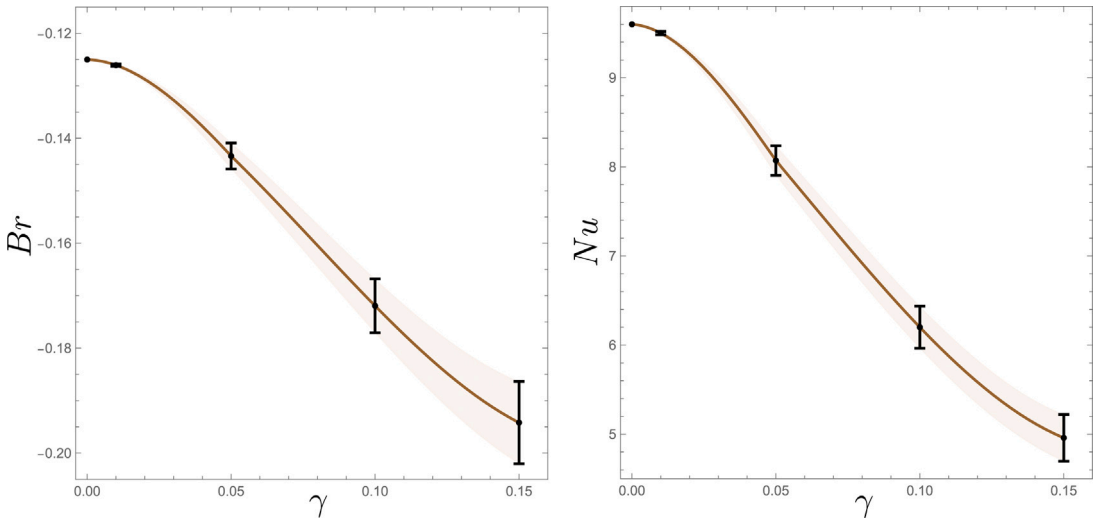

Fig. 8. Values of Br and Nu versus γ for the T boundary condition: average values (black dots) with 1 standard deviation range (black segments).

Nu is 9.6. Thus, an increasing roughness yields an increasing $|Br|$ and a decreasing Nu. The latter effect is due to the, already pointed out, less efficient wall heat transfer when the relative roughness γ grows. The increasing $|Br|$ as the roughness increases is a dual effect to the decreasing Nusselt number. In fact, while Nu is proportional to the wall heat flux, Br is inversely proportional to that quantity.

Figs. 9 and 10 illustrate the effects of roughness on the values of Nu for the H1 and H2 boundary conditions. The two different boundary conditions are identified by different colours: blue for H1 and red for H2. Fig. 9 is relative to $Br \geq 0$, with $Br = 0.1, 1, 10$ and the case $Br \to 0$ reported for comparison, while Fig. 10 is for $Br \leq 0$. Positive Brinkman numbers address situations where the microchannel wall is externally heated, while negative Brinkman numbers describe microchannels with an externally cooled wall. It is evident from Figs. 9 and 10, that the effects of surface roughness are utterly different with heating and cooling, for every prescribed $|Br|$. Fig. 9 shows that an increasing roughness yields a decreasing Nu, with the values for the H1 conditions slightly larger than those for the H2 conditions. The distinction between H1 and H2 boundary conditions tends to become statistically negligible when Br increases. Fig. 10 shows cases where $Br = -0.1, -1, -10$, with the case $Br \to 0$ reported again for an easier comparison. The first evident feature revealed by Fig. 10 is that, when Br is negative and $|Br|$ is large enough, the Nusselt number is negative. The meaning can be gathered from (9) and (14): a negative Nu means wall cooling with $T_w > T_b$. Such a situation may arise when the viscous dissipation effect becomes so intense that the wall cooling is insufficient to prevent a streamwise increase of the fluid temperature. In the limiting case of zero wall roughness, $\gamma \to 0$, (25) shows that $Nu < 0$ when $Br < -11/48 \approx -0.229$. Coherently, Fig. 10 reveals negative values of Nu for $Br = -1$ and $Br = -10$, but not for $Br = -0.1$. In general, Fig. 10 confirms that the increasing wall roughness means a less efficient wall heat transfer. However, there is an atypical behaviour revealed for the case $Br = -1$ which could be considered a non-monotonic response of Nu versus γ. However, the relatively large standard deviations reduce the statistical support for such a conclusion. Finally, it is worth reporting that the monotonic trend of Nu versus γ shown in the frame with $Br = -10$ means a less efficient wall heat transfer. In fact, this frame shows that $|Nu|$ decreases with γ. The cases $Br = \pm 10$ reported in Figs. 9 and 10 show statistically identical Nu for the H1 and H2 boundary conditions, but the Nusselt number values are indeed very small. When $\gamma \to 0$, this claim is coherent with (25) for $|Br| \gg 11/48$.

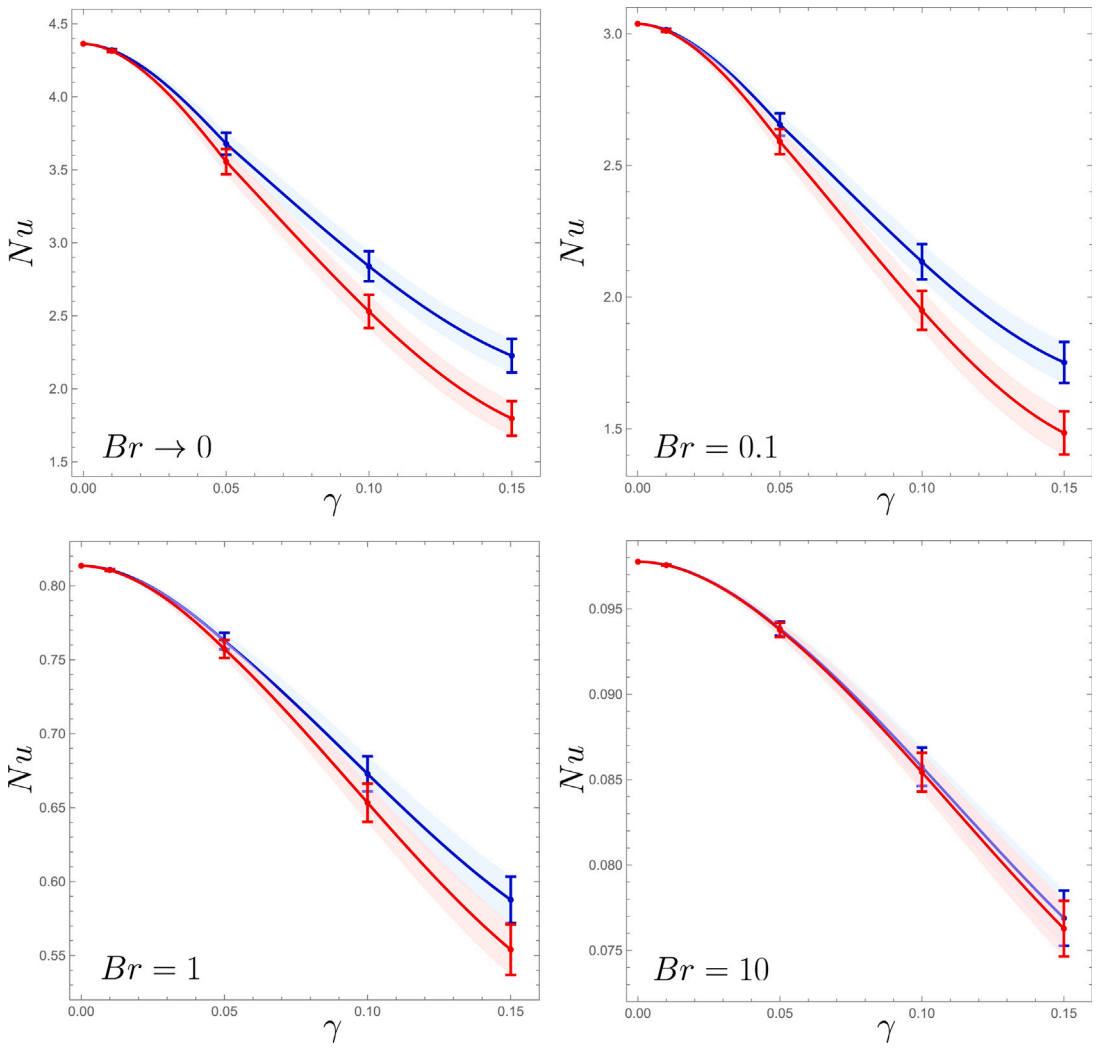

Fig. 9. Values of Nu versus γ for the H1 (blue) and the H2 (red) boundary conditions with different values of $Br \geq 0$: average values with 1 standard deviation range.

Table 2
Case study (Section 4.3): values of Br for air and CO_2 with different Reynolds numbers and heating ($\dot{Q} > 0$) or cooling ($\dot{Q} < 0$) conditions.

Re	air ($\dot{Q} = \pm 30$ mW)	CO_2 ($\dot{Q} = \pm 30$ mW)	air ($\dot{Q} = \pm 50$ mW)	CO_2 ($\dot{Q} = \pm 50$ mW)
1000	± 0.7	± 0.3	± 0.4	± 0.2
1500	± 1.5	± 0.6	± 0.9	± 0.4

4.3. Case study of a thermal process

Applications of the heat transfer and flow characteristics of microchannels emerge in the design of micro-electromechanical systems (MEMS) and in their use for micro heat exchangers, biomedical devices and fuel cells where the control of thermal processes is an important target. The class of thermal processes considered in our analysis so far have been explored experimentally by many authors.

An interesting example is suggested via the experimental data reported by Lin et al. [21] where gas flows of air or CO_2 in microtubes are studied. These authors employed electro-deposition of nickel on an aluminum substrate for the fabrication of microtubes with inner diameter of 0.5 mm and a uniform surface roughness up to 9.3 μm. This means a value of relative roughness $\gamma \approx 0.04$. As shown by Figs. 7 and 8, this value of γ leads to the prediction of an increase in the Poiseuille number around 3% and a decrease of the Nusselt number for the T boundary condition around 11% relative to a smooth tube ($\gamma = 0$). In fact, in this case, the absolute value of the Brinkman number is approximately 0.14, meaning an increase in the effect of viscous dissipation around 12% with respect to a smooth tube.

For the H1 and H2 thermal boundary conditions, one may evaluate possible values of the Brinkman number relative to heating or cooling conditions defined by the sign of the thermal power supplied to the wall, $\dot{Q}$. With $r_0 = 0.25$ mm and a 20 cm long microtube, one obtains the data reported in Table 2. The values of the Reynolds number are relative to the laminar flow regime as defined in Lin et al. [21], namely $Re < 2000$.

5. Conclusions

The laminar forced convection in a circular microchannel has been investigated by considering the effect of viscous dissipation and by modelling the wall roughness. The wall roughness has been assumed to affect the cross-sectional geometry in a random way within a range of $\pm \gamma r_0$, where r_0 is the duct radius and $0 \leq \gamma < 1$. The surface roughness model adopted here has been conceived by the tacit assumption that

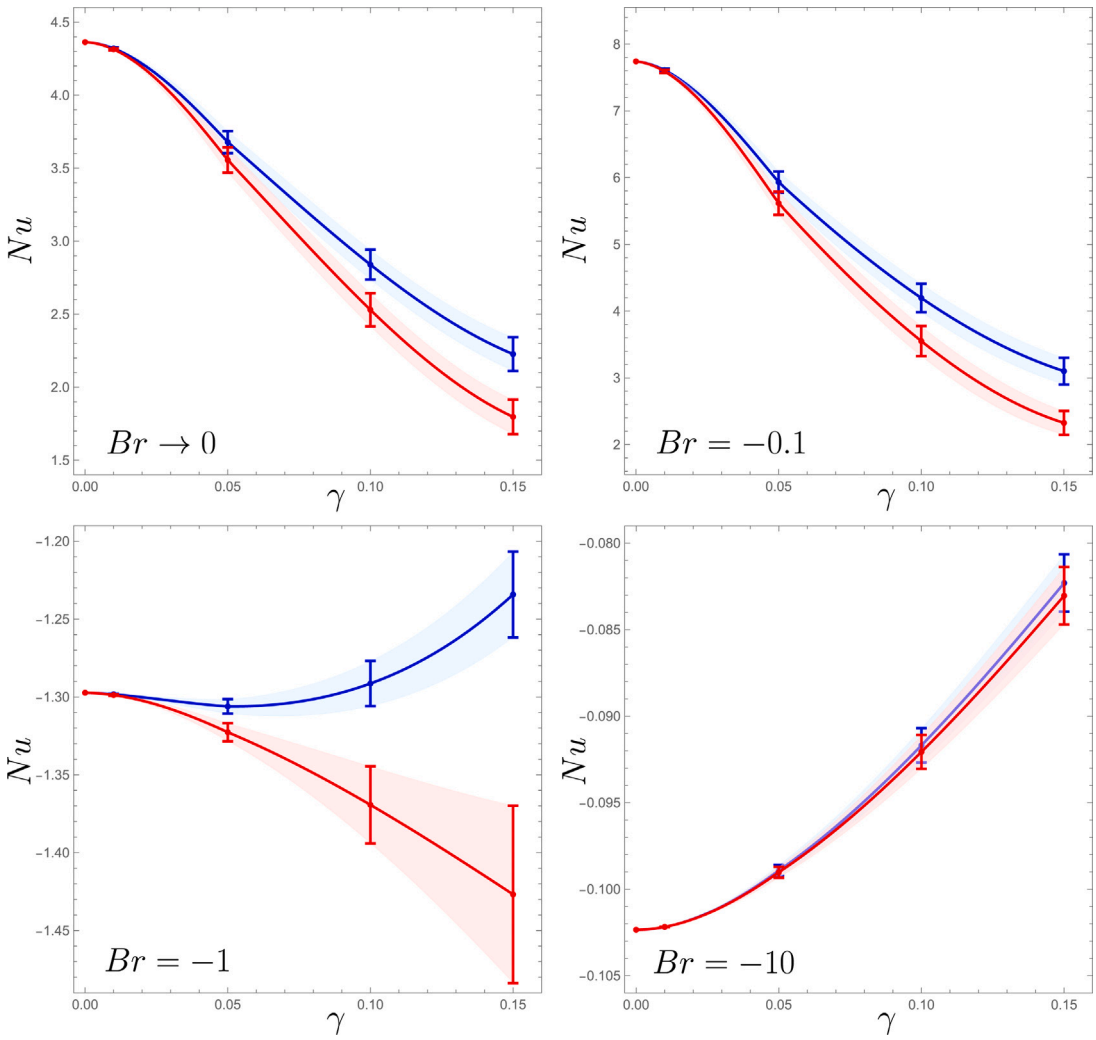

Fig. 10. Values of Nu versus γ for the H1 (blue) and the H2 (red) boundary conditions with different values of $Br \leq 0$: average values with 1 standard deviation range.

the technology employed for the microchannel fabrication is such that the radial changes in the wall geometry are significantly larger than the axial changes.

A statistical sample of 100 different microchannels has been generated as computational domains to be employed for the solution of the governing equations. In each instance of the statistical sample, all the three standard thermal boundary conditions, T, H1 and H2, have been considered in order to evaluate the Nusselt number Nu and the Poiseuille number σ. The comparison between the actual microchannel and the smooth circular duct has revealed a larger Poiseuille number and a smaller Nusselt number in the rough walled microchannel.

The effect of viscous dissipation, whose intensity is expressed by the Brinkman number Br, acts differently for wall heating $Br > 0$ or wall cooling $Br < 0$. In the former case, the Nusselt number is always positive and the values of Nu for the H1 and H2 boundary conditions turn out to be statistically different when Br is small and the wall roughness γ is large enough. As $Br > 0$ becomes large, the values of Nu for the H1 and H2 conditions become statistically coincident. The behaviour of the Nusselt number is different when $Br < 0$, as Nu is negative when the absolute value of the Brinkman number becomes large enough. Furthermore, the evaluated mean values of Nu over the statistical sample may display non-monotonic trends versus γ, at intermediate values of $|Br|$, even if the reliability of such trends is questionable due to the relatively large standard deviations of such data.

An improvement of this analysis can be sought by including effects of wall slip that may be specially important when gas flows at low density are examined. A much more complicated aspect, yet to be developed, is the model of a geometry where the wall roughness is not only in the circumferential direction, but also in the streamwise direction. In fact, such a possibility of a three-dimensional wall roughness has been explored by other authors [12,15,19,22]. On the other hand, three-dimensional surface roughness is disregarded in the present analysis.

Declaration of competing interest

The authors declare that they have no known competing financial interests or personal relationships that could have appeared to influence the work reported in this paper.

Acknowledgments

The work was supported by Alma Mater Studiorum Università di Bologna, Italy, grant number RFO-2023.

Data availability

No data was used for the research described in the article.

References

[1] O.K. Siddiqui, S.M. Zubair, Efficient energy utilization through proper design of microchannel heat exchanger manifolds: A comprehensive review, Renew. Sustain. Energy Rev. 74 (2017) 969–1002.

[2] N. Gilmore, V. Timchenko, C. Menictas, Microchannel cooling of concentrator photovoltaics: A review, Renew. Sustain. Energy Rev. 90 (2018) 1041–1059.

[3] Z. Akbari, M.A. Raoufi, S. Mirjalali, B. Aghajanloo, A review on inertial microfluidic fabrication methods, Biomicrofluidics 17 (2023).

[4] K. Imaizumi, A. Fujita, A. Suzuki, M. Kobashi, M. Kato, Additive manufacturing for 3d microchannel structure using La(FexSi1-x)13 magnetic refrigerant via laser powder bed fusion, Addit. Manuf. 83 (2024) 104076.

[5] B. Xu, K.T. Ooi, C. Mavriplis, M.E. Zaghloul, Evaluation of viscous dissipation in liquid flow in microchannels, J. Micromech. Microeng. 13 (2002) 53.

[6] J. Koo, C. Kleinstreuer, Viscous dissipation effects in microtubes and microchannels, Int. J. Heat Mass Transfer 47 (2004) 3159–3169.

[7] J. Van Rij, T. Ameel, T. Harman, The effect of viscous dissipation and rarefaction on rectangular microchannel convective heat transfer, Int. J. Therm. Sci. 48 (2009) 271–281.

[8] C. Nonino, S. Del Giudice, S. Savino, Temperature-dependent viscosity and viscous dissipation effects in microchannel flows with uniform wall heat flux, Heat Transf. Eng. 31 (2010) 682–691.

[9] D. Jing, Y. Pan, X. Wang, Joule heating, viscous dissipation and convective heat transfer of pressure-driven flow in a microchannel with surface charge-dependent slip, Int. J. Heat Mass Transfer 108 (2017) 1305–1313.

[10] S. Mukherjee, P. Biswal, S. Chakraborty, S. DasGupta, Effects of viscous dissipation during forced convection of power-law fluids in microchannels, Int. Commun. Heat Mass Transfer 89 (2017) 83–90.

[11] S. Prakash, S. Kumar, Fabrication of microchannels: a review, Proc. Inst. Mech. Eng. B 229 (2015) 1273–1288.

[12] H. Wang, Y. Wang, Influence of three-dimensional wall roughness on the laminar flow in microtube, Int. J. Heat Fluid Flow 28 (2007) 220–228.

[13] M.B. Turgay, A.G. Yazicioglu, Effect of surface roughness in parallel-plate microchannels on heat transfer, Numer. Heat Transf. Part A: Appl. 56 (2009) 497–514.

[14] G. Croce, P. D'agaro, C. Nonino, Three-dimensional roughness effect on microchannel heat transfer and pressure drop, Int. J. Heat Mass Transfer 50 (2007) 5249–5259.

[15] G. Croce, P. D'Agaro, Numerical simulation of roughness effect on microchannel heat transfer and pressure drop in laminar flow, J. Phys. D: Appl. Phys. 38 (2005) 1518–1530.

[16] G.P. Celata, M. Cumo, M. Guglielmi, G. Zummo, Experimental investigation of hydraulic and single-phase heat transfer in 0.130-mm capillary tube, Microscale Thermophys. Eng. 6 (2002) 85–97.

[17] R.K. Shah, A.L. London, Laminar flow forced convection in ducts, in: Advances in Heat Transfer, Academic Press, 1978.

[18] A. Barletta, Fully developed laminar forced convection in circular ducts for power-law fluids with viscous dissipation, Int. J. Heat Mass Transfer 40 (1996) 15–26.

[19] N. Pelević, T.H. van der Meer, Heat transfer and pressure drop in microchannels with random roughness, Int. J. Therm. Sci. 99 (2016) 125–135.

[20] G. Croce, P. D'Agaro, Numerical analysis of roughness effect on microtube heat transfer, Superlattices Microstruct. 35 (2004) 601–616.

[21] T.-Y. Lin, C.-W. Chen, C.-Y. Yang, S.G. Kandlikar, An experimental investigation on friction characteristics and heat transfer of air and CO2 flow in microtubes with structured surface roughness, Heat Transf. Eng. 35 (2014) 150–158.

[22] H. Lu, M. Xu, L. Gong, X. Duan, J.C. Chai, Effects of surface roughness in microchannel with passive heat transfer enhancement structures, Int. J. Heat Mass Transfer 148 (2020) 119070.